Real-Time Diagnosis Based on Signal Convolution-Pooling Processing and Shared Filter Learning for Transistor Open-Circuit Faults in a T-Type Inverter

Borong Wang, *Member, IEEE*, Guodong Chen, Jinfeng Song, Chenyi Peng, Philip T. Krein, *Life Fellow, IEEE*, and Hao Ma, *Senior Member, IEEE*

***Abstract*—This article proposes a data-driven method based on signal convolution pooling for real-time fault diagnosis in T-type inverters. The model is composed of an auxiliary neural network and a multilayer convolution feature classifier (MCFC). The auxiliary neural network can learn and provide filter parameters for an MCFC by learning from a small training dataset. Through shared filter learning and a global average pooling layer, a feedforward MCFC can greatly reduce testing time. This makes the approach suitable for real-time fault diagnosis. A feature processing function is used to retain fault features observed in the measured three-phase current signals while avoiding the effects of load changes. A multisignal sequence reconstruction strategy is proposed to transform multiple time-series diagnostic signals into an input feature map for the MCFC. This strategy extends the domain of the MCFC information by increasing the input channel count of the auxiliary neural network. The combined approach increases fault diagnosis accuracy compared to prior work. The performance of the proposed diagnosis method is validated with experiments.**

***Index Terms*—Convolution-pooling model, filter parameter sharing, open-circuit (OC) faults, real-time fault diagnosis, T-type inverters.**

I. Introduction

T-TYPE inverters, emerging as high-performance multilevel converters, have the merits of good harmonic characteristics, reduced *dv/dt*, and high efficiency [1], [2], [3]. Compared with the two-level inverters, T-type three-level ($T^2$3L) inverters have more power semiconductors and this is a challenge for reliable operation [4]. The research effort presented here seeks to apply signal convolution-pooling methods and neural-network methods for learning circuit and fault behavior to enhance and accelerate fault diagnosis in these inverters.

Manuscript received 13 August 2023; revised 22 December 2023; accepted 26 January 2024. Date of publication 6 February 2024; date of current version 20 March 2024. This work was supported by the Zhejiang University/University of Illinois at Urbana-Champaign Institute. Recommended for publication by Associate Editor K. B. Park. *(Corresponding author: Hao Ma.)*

Borong Wang, Guodong Chen, Jinfeng Song, and Chenyi Peng are with the Technology Center, Shanghai Electric Power Transmission and Distribution Group, Shanghai 20042, China (e-mail: wangbr@shanghai-electric.com; chengd@shanghai-electric.com; songjf@shanghai-electric.com; pengchy2@shanghai-electric.com).

Philip T. Krein is with the Zhejiang University/University of Illinois at Urbana-Champaign Institute, Haining 314400, China, and also with the University of Illinois at Urbana-Champaign, Urbana, IL 61801 USA (e-mail: krein@illinois.edu).

Hao Ma is with the Zhejiang University/University of Illinois at Urbana-Champaign Institute, Haining 314400, China, and also with the College of Electrical Engineering, Zhejiang University, Hangzhou 310027, China (e-mail: mahao@zju.edu.cn).

Color versions of one or more figures in this article are available at https://doi.org/10.1109/TPEL.2024.3362365.

Digital Object Identifier 10.1109/TPEL.2024.3362365

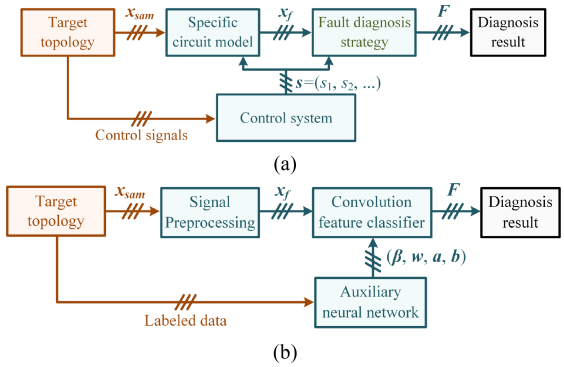

Fig. 1. Diagram of (a) circuit-model-based diagnosis strategy and (b) proposed data-driven-based diagnosis strategy.

Open-circuit (OC) faults are relatively common in power semiconductor devices. OC faults will degrade system performance and ultimately have catastrophic consequences. Here, we seek to improve OC-fault diagnosis performance in terms of target model parameter dependence and fault detection speed. The diagnostic system can be applied to $T^2$3L inverters to monitor operating status online and provide fast, reliable fault locations. The objective is to achieve seamless fault recovery by dynamic circuit configuration. This method can meet expectations with limited circuit information and does not require complex diagnosis rules.

Power transistor OC-fault diagnosis for inverters has been studied widely. Prior current- and voltage-sensing methods require the detailed analysis of state variables [5], [6], [7], [8], [9], [10], [11], [12], [13] and accurate modeling of target circuit modes [14], [15], [16] to track the operating states. A diagram summarizing typical circuit-model-based fault diagnosis is shown in Fig. 1(a), where sampling signals $\boldsymbol{x}_{sam}$ can be transformed into specific state variables $\boldsymbol{x}_f$ based on model and control variables to represent circuit states. Features in $\boldsymbol{x}_f$ signals

associated with faults can be determined to identify a fault location through a diagnosis strategy. Circuit-model methods can generate acceptable diagnostics. For multilevel inverters, the logical framework to implement them is complicated. Sensitivity to parameters and selection of suitable thresholds are important to ensure robustness and accuracy of fault diagnosis.

To handle these issues, a data-driven method based on a convolution-pooling model is presented here. As shown in Fig. 1(b), a convolution feature classifier can extract abnormal features in data by means of trained filter parameters (β, $\boldsymbol{w}$, $\boldsymbol{a}$, $\boldsymbol{b}$) from an auxiliary neural network. Based on abnormal features, corresponding fault indication signals $\boldsymbol{F}$ can be obtained. Compared with Fig. 1(a), the proposed data-driven method tracks circuit operating modes by selecting suitable filter parameters even when the circuit model is inaccurate. The diagnosis strategy in Fig. 1(b) is not limited to a specific topology. The auxiliary neural network will need to be built to handle the number of transistors and fault scenarios to be considered. The size of a convolution feature classifier would be adjusted based on shared filter parameters to distinguish fault features. Signal preprocessing and parameter sharing are similar for various topologies and applications.

Data-driven methods for feature extraction and classification are emerging. These include artificial neural networks (ANNs), K-nearest neighbor networks, support vector machines (SVMs), and others [17], [18], [19]. Effective data-driven methods can extract circuit operating characteristics without models, potentially reducing the difficulty of diagnostic system development. ANNs, nonlinear networks with multiple inputs and outputs, can simulate a map between converter inputs and outputs. Bernieri et al. [20] investigate ANN applications for fault diagnosis and system identification. Compared with other data-driven methods, ANNs have a high degree of freedom for solving nonlinear systems and preserve object characteristics without expert knowledge. An error backpropagation algorithm could be applied to an ANN to enhance its capability to approximate nonlinear mappings. Such a back propagation neural network (BPNN) can learn the target fault behavior accurately by correcting network parameters [21]. ANNs can also be combined with signal processing strategies, such as principal component analysis, fast Fourier transforms (FFT), and discrete wavelet transforms to enhance diagnosis accuracy and robustness [22], [23], [24].

A three-layer BPNN and an FFT were employed to detect OC faults in single-phase neutral point clamped (NPC) inverters in [25]. In [26], multistate data processing and subsection fluctuation analysis were proposed to distinguish features in current signals. A BPNN block was employed to determine faulty devices in photovoltaic inverters. A multiple-class neural network comprising multiple small-scale ANNs was presented in [27]. Faults in two-level inverters could be detected within 20 ms. Li et al. [28] achieved fast real-time diagnosis based on a BPNN but relied on the accurate circuit model. Feature extraction capability in complicated systems will be limited in these methods because of their shallow network structure [29]. Multilevel inverters have more operating modes and some OC faults have similar responses. In these cases, diagnostic accuracy can be improved with extended models or by increasing the processed data quantity. These methods are effective for offline analysis, but they may be less suitable for online fault diagnosis because of the complex processing of a large amount of data. To accelerate diagnostic speed, a relatively shallow BPNN will be used here.

Alternatively, deep learning methods have the potential to extract features of a complex system from large-scale datasets. Some deep learning methods, such as long short-term memory neural networks (LSTMNN) and deep residual networks, were presented in [30] and [31], and applied there to fault diagnosis. An attention collaborative stacked LSTMNN was proposed in [32] for fault diagnosis of an NPC inverter. It was robust under various noise conditions. For online multiple-OC-fault diagnosis of $T^2$3L inverters, a multimodal deep residual filter network (DRFN) was established in [33], and OC faults there were located within 21 ms.

Convolutional neural networks (CNNs) have been discussed in the context of deep learning. They were applied originally to image recognition. CNNs have powerful feature extraction capabilities while using fewer parameters compared with other deep learning methods [34]. A CNN can infer information among sampled signals in a given time interval, seeking to fully mine relationships among local features. Compared with BPNNs, CNNs can improve feature identification accuracy. In [35], a diagnosis method was proposed for modular multilevel converters based on a 1-D CNN. That approach employed raw voltage and current data to achieve fault identification within 100 ms. A CNN-based method was proposed in [36] for fault diagnosis in active neutral point clamped (ANPC) inverters by extracting features of distorted currents. In [35] and [36], multiple fully connected layers were adopted. The approach required extensive training to obtain the accurate parameters. Different convolution layers in a CNN can share weights to reduce training parameters, but signal preprocessing time is still long [37], [38]. In [39], an unsupervised CNN method was presented for induction motor fault diagnosis. The network could extract features directly from unlabeled datasets by means of feedforward signal processing. Parameters obtained from a separate neural network were provided to the CNN to enhance model robustness and fault discrimination. However, powerful CNN feature extraction capabilities were underused because of 1-D feature maps and incomplete learning results.

Existing neural-network methods for inverter OC-fault diagnosis are still complex, which implies that many network parameters need to be set. This leads to a need for large, high-quality, labeled training datasets, which are not likely to be available for practical inverters. A complex network model will prolong diagnostic processing duration. Due to these issues, neural networks have been difficult to apply to online monitoring of inverter systems when quick response time is needed. In this article, a convolution-pooling model with shared filter learning is proposed to provide real-time fault diagnosis without relying on the accurate circuit parameters. The model differs from conventional CNNs: here, the fully connected layer, associated with most of the weight parameters, is omitted to avoid complex training and data processing. This model can

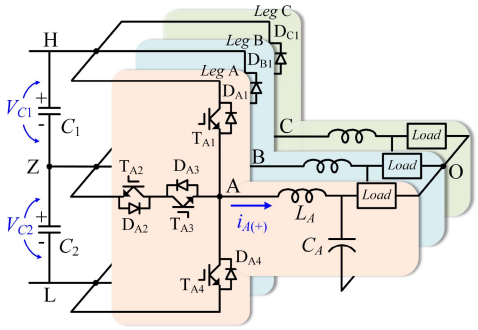

Fig. 2. Diagram of the three-phase T^{2}3L inverter system.

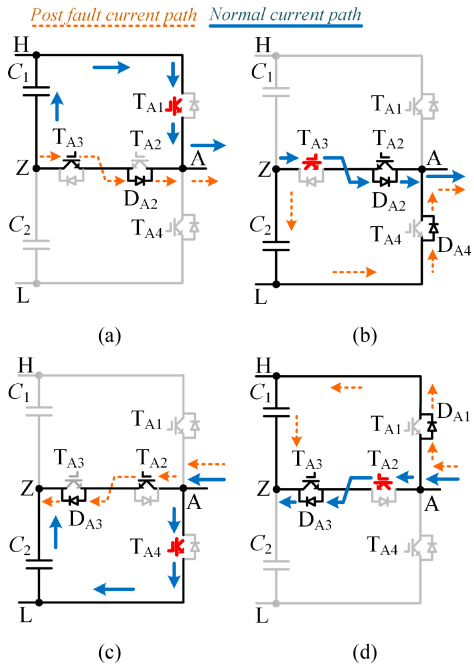

Fig. 3. Current paths formed under (a) T_{A1} OC fault, (b) T_{A3} OC fault, (c) T_{A4} OC fault, and (d) T_{A2} OC fault.

shorten fault location time to less than 3.6 ms, far less than one mains frequency cycle. It makes use of current signals from the controller and does not require extra sensors.

The contributions here are as follows.

1) By sharing filter parameters learned from a simple BPNN, the proposed multilayer convolution feature classifier (MCFC) can distinguish fault features more effectively than the BPNN alone. The MCFC can function with a small number of training samples.
2) A current-decay-component-based processing method is proposed to highlight abnormal changes in current signals and improve MCFC diagnostic accuracy.
3) The MCFC employs a global average pooling (GAP) layer to reduce the dimension of its convolved output feature maps in place of a fully connected layer and local pooling operation. Fault features are extracted based on a feed-forward architecture with a GAP layer, greatly reducing computational complexity. The MCFC is shown to achieve fast real-time diagnosis.
4) To integrate three-phase time-series current signals into a feature map for convolution, a multisignal sequence reconstruction (MSSR) approach is proposed. This allows the MCFC to comprehensively evaluate the three-phase operating status in a given interval and enhances fault extraction capability by expanding the domain of diagnostic information.

II. Analysis and Extraction of Fault Features

This section summarizes the characteristics of transistor faults in T^{2}3L inverters and optimizes sampling variables for diagnostics. Selected diagnosis signals are independent of the circuit model.

Fig. 2 shows a T^{2}3L inverter. C_1 and C_2 in series form the dc-link capacitors, which split the input voltage $V_{\rm dc}$, and provide a neutral point Z. Power transistors T_{X1} and T_{X4} ($X = A, B, C$) connect to the positive and negative dc bus, respectively, and are defined here as half-bridge transistors. T_{X2} and T_{X3}, defined as middle transistors, form a bidirectional switch between neutral point Z and the legs. D_{X1}–D_{X4} are the corresponding antiparallel body diodes. Define s_{X1}–s_{X4} as switching signals of T_{X1}–T_{X4}. The output pole voltages V_{XZ} are

$$V_{XZ} = \frac{1}{2}V_{\rm dc}(S_X - 1) \tag{1}$$

$$S_X = \begin{cases} 2 & (s_{X1},\ s_{X2},\ s_{X3},\ s_{X4}) = (1,\ 0,\ 1,\ 0) \\ 1 & (s_{X1},\ s_{X2},\ s_{X3},\ s_{X4}) = (0,\ 1,\ 1,\ 0) \\ 0 & (s_{X1},\ s_{X2},\ s_{X3},\ s_{X4}) = (0,\ 1,\ 0,\ 1). \end{cases} \tag{2}$$

V_{XZ} can be $0.5V_{\rm dc}$, 0, or $-0.5V_{\rm dc}$, when S_X is equal to 2, 1, and 0, respectively, corresponding to operating states [P], [O], and [N].

Based on current paths through various transistors, the behavior of phase A can be described by four operating modes, as shown in Fig. 3. Assuming a balanced three-phase load with per-phase impedance Z_o, three-phase currents under normal conditions are

$$\begin{bmatrix} i_A^* \\ i_B^* \\ i_C^* \end{bmatrix} = \frac{1}{Z_o}\begin{bmatrix} V_{AO}^* \\ V_{BO}^* \\ V_{CO}^* \end{bmatrix} = \frac{1}{Z_o}\begin{bmatrix} 2 & -1 & -1 \\ -1 & 2 & -1 \\ -1 & -1 & 2 \end{bmatrix}\begin{bmatrix} V_{AZ}^* \\ V_{BZ}^* \\ V_{CZ}^* \end{bmatrix} \tag{3}$$

where i_X^* denotes the normal phase current, V_{XO}^* refers to the normal voltage between each phase output pole X to the load common terminal O, and V_{XZ}^* is the normal voltage between each phase output pole X to a neutral point Z.

When T_{A1} fails, positive current only flows through T_{A3} and D_{A2} in Fig. 3(a), and the operating state changes from [P] to [O]. Fig. 3(b) shows that T_{A3} OC faults can cause the current to flow through D_{A4}, and the operating state becomes [N] instead of [O]. In these cases, V_{AZ} decreases and i_A reduces due to undesired operating states. Similarly, V_{AZ} will increase if T_{A2} or T_{A4} fails during the negative half cycle of i_A in Fig. 3(c) and

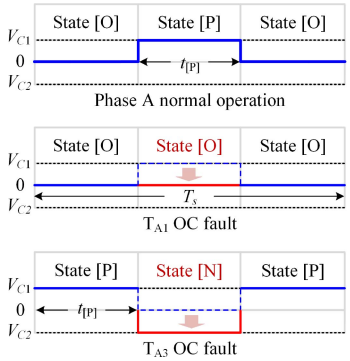

Fig. 4. Variation of output pole voltages under normal, T_{A1} OC-fault, and T_{A3} OC-fault conditions.

(d). The output star connection requires $i_A + i_B + i_C = 0$. Thus, i_B and i_C will be affected by i_A distortion.

Taking an OC fault of T_{A1} as an example, the postfault currents $i_{X.F}$ in phase A become

$$\begin{bmatrix} i_{A.F} \\ i_{B.F} \\ i_{C.F} \end{bmatrix} = \begin{bmatrix} i_A^* + \Delta i_{A.F} \\ i_B^* + \Delta i_{B.F} \\ i_C^* + \Delta i_{C.F} \end{bmatrix} = \frac{1}{Z_o} \begin{bmatrix} 2 & -1 & -1 \\ -1 & 2 & -1 \\ -1 & -1 & 2 \end{bmatrix} \begin{bmatrix} V_{AZ}^* + \Delta V_{AZ} \\ V_{BZ}^* \\ V_{CZ}^* \end{bmatrix}. \quad (4)$$

In (4), the variation of postfault current $\Delta i_{X.F}$ can be derived from the output pole voltage deviation (ΔV_{AZ}), and ΔV_{XZ} is determined by an undesired state transition, as shown in Fig. 4.

Based on (4) and Fig. 4, the average value of $\Delta i_{X.F}$ over a switching period is

$$\begin{bmatrix} \Delta i_{A.F\_ave} \\ \Delta i_{B.F\_ave} \\ \Delta i_{C.F\_ave} \end{bmatrix} = \frac{-V_{\rm dc} t_{[P]}}{2T_s Z_o} \begin{bmatrix} 2 \\ -1 \\ -1 \end{bmatrix} = \frac{d_{A(+)}}{2Z_o} \begin{bmatrix} -2V_{\rm dc} \\ V_{\rm dc} \\ V_{\rm dc} \end{bmatrix} \quad (5)$$

where $d_{A(+)}$ refers to the duty cycle of the state [P] in phase A. The change $\Delta i_{X.F\text{ave}}$ in response to a T_{A3} fault is

$$\begin{bmatrix} \Delta i_{A.F\_ave} \\ \Delta i_{B.F\_ave} \\ \Delta i_{C.F\_ave} \end{bmatrix} = \frac{-V_{\rm dc}(T_s - t_{[P]})}{2T_s Z_o} \begin{bmatrix} 2 \\ -1 \\ -1 \end{bmatrix} = \frac{1 - d_{A(+)}}{2Z_o} \begin{bmatrix} -2V_{\rm dc} \\ V_{\rm dc} \\ V_{\rm dc} \end{bmatrix} \quad (6)$$

and a similar analysis applies to other fault conditions.

Following from (5) and (6), distorted currents with a transistor fault are related to the duration of unreachable state [P]. The duration of state [P] will increase as the amplitude of phase current increases. Current decay is less when a middle transistor (T_{X2} or T_{X3}) fails near a current peak, and the undesired change of phase currents is not obvious if a half-bridge transistor (T_{X1} or T_{X4}) fails near the current zero-crossing point. Thus, the distorted ac component at the specific moment of fault might be difficult to distinguish and may be evident only through "microfault" features—subtle effects on waveform decay.

Given that some changes will be small, feature processing is needed to extract current-decay components. First, the three-phase sampled current signals are normalized into the range $[-1, 1]$ based on

$$i_{X.N}[n] = \text{Nor}(i_X[n]) = \frac{i_X[n]}{\sqrt{i_d^2[n] + i_q^2[n]}} \quad (7)$$

to eliminate the effects of loads or modulation indices. Here, $i_X[n]$ denotes the value of i_X in the nth cycle. Currents i_d and i_q denote current components in a stationary reference frame

$$\begin{bmatrix} i_d \\ i_q \end{bmatrix} = \frac{2}{3} \begin{bmatrix} \sin(\omega t + \phi_A) & \sin(\omega t + \phi_B) & \sin(\omega t + \phi_C) \\ \cos(\omega t + \phi_A) & \cos(\omega t + \phi_B) & \cos(\omega t + \phi_C) \end{bmatrix} \begin{bmatrix} i_A \\ i_B \\ i_C \end{bmatrix} \quad (8)$$

where ϕ_X denotes the initial phase angle, and ω refers to the current fundamental frequency.

Next, normalized current signals $i_{X.N}$ are subjected to decay acceleration processing that highlights the decay degree of fault current components

$$i_{X.N3}[n] = \text{Nor}(i_X^3[n]) = \left(\frac{i_X^2[n]}{i_d^2[n] + i_q^2[n]} \right)^{3/2} \quad (9)$$

so that decay characteristics in different fault scenarios are made more distinguishable. The cubic form maintains sign information about current polarity while amplifying the detection of fault currents.

Based on (9), Fig. 5 shows the waveforms of calculated $i_{X.N3}$ and phase currents $i_{X.N}$ under several fault scenarios. Distortion in $i_{X.N3}$ is readily observed under these fault conditions. Fig. 6 shows time derivatives of current signals ($i_{A.N}$, $i_{A.N2}$, $i_{A.N3}$, $\phi_A = 0$) during the positive half cycle. The absolute rate of change of $i_{A.N3}$ is higher than for $i_{A.N}$ throughout most of the half cycle. Thus, the decay rate of $i_{A.N3}$ is greater than that of $i_{A.N}$ when phase current i_A is distorted due to an OC fault, and this can be used to advantage to amplify the fault characteristics. In the proposed fault diagnosis method, $i_{A.N3}$, $i_{B.N3}$, and $i_{C.N3}$ are regarded as input diagnosis signals for the MCFC framework. A detail is that an MCFC is intended to filter and extract fault features in the form of 2-D data maps. To obtain effective diagnosis results, it is necessary to transform $i_{A.N3}$, $i_{B.N3}$, and $i_{C.N3}$ from 1-D time-series signals into 2-D feature maps. A method for feature map construction will be presented in Section IV.

III. Construction of Proposed Convolution-Pooling Diagnosis Model

A framework of the proposed convolution-pooling model is shown in Fig. 7 . In this model, a three-layer BPNN serves as an auxiliary neural network to learn and train filter parameters. Parameters learned by this BPNN are shared with the MCFC. The MCFC, as a special CNN, can extract abnormal features from diagnosis signals to identify fault modes. The function of the proposed framework and the principles of filter parameter sharing are analyzed in this section.

A. Auxiliary Neural Network and MCFC

The auxiliary neural network is shown in Fig. 8. Each layer consists of several neurons that serve as the basic data processing

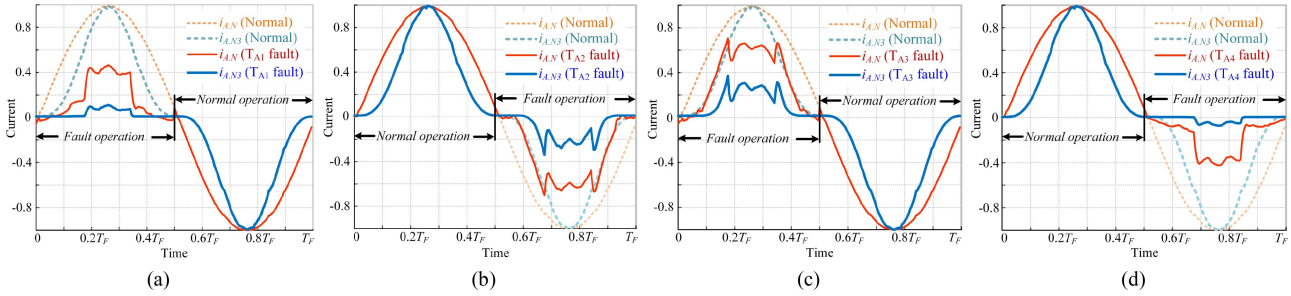

Fig. 5. Waveforms of current variables under (a) T_{A1} OC fault, (b) T_{A2} OC fault, (c) T_{A3} OC fault, and (d) T_{A4} OC fault.

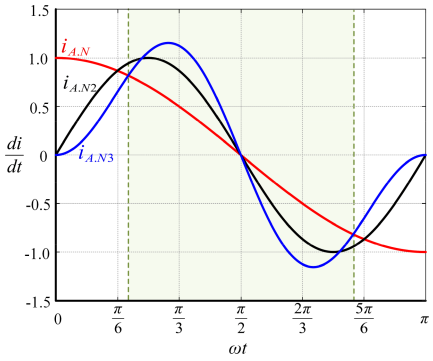

Fig. 6. Time derivatives of current signals.

units. In the forward propagation process to the next layer, the output data of the hidden layer can be represented as

$$z_j = f_{\text{hid}}(y_j) = f_{\text{hid}}\left(\sum_{n=1}^{r} \beta_{j,n}^{(\text{hid})} x_n + a_j\right) \tag{10}$$

where x_n denotes the input data to the nth input layer neuron, z_j refers to the data output from the jth neuron in the hidden layer, $\beta_{j,n}^{(\text{hid})}$ denotes the connection weights between the nth neuron in the input layer and the jth neuron in the hidden layer, a_j denotes a bias term, which can be regarded as a threshold setting, and $f_{\text{hid}}(\cdot)$ is an activation function within the hidden layer. Similarly, the data propagation between the hidden and output layers can be represented by

$$o_l = f_{\text{out}}\left(\sum_{k=1}^{p} \beta_{l,k}^{(\text{out})} z_k + b_l\right) \tag{11}$$

where o_l denotes the output data from the lth neuron in the output layer and $f_{\text{out}}(\cdot)$ is an activation function of the output layer.

In this method, preprocessed diagnostic signals $i_{A.N3}$, $i_{B.N3}$, and $i_{C.N3}$ are fed into the input layer. The inverter operating status under normal and various transistor OC-fault conditions are defined as *target categories*. The ANN output results map circuit behavior into one of the target categories 1 to g to identify system abnormal operation. To classify output data into these categories, the output layer is followed by a *Softmax* layer, adapted from prior use in pattern recognition [28].

To learn object characteristics, the system in Fig. 8 would be trained on normal and faulted operating conditions by error backpropagation to adjust parameters (β, $\boldsymbol{a}$, $\boldsymbol{b}$). In conventional practice, the output error of the auxiliary neural network is often calculated by a cross-entropy loss function to reflect differences among probability distributions [40].

The MCFC is a special CNN consisting of a convolution layer, a GAP layer, and a *Softmax* layer. The convolution layer extracts representative information from input data by means of convolution kernels [41]. Fig. 9 shows the operation of convolution layers, where the input feature map ($\boldsymbol{x_k}$) is convolved with feature filters ($\boldsymbol{w}_l$) to generate new feature maps ($\boldsymbol{z}_l$) as inputs to the next layer. This operation can be expressed as

$$\boldsymbol{z}_l = f_{\text{conv}}\left(\sum_{k=1}^{K} \boldsymbol{w}_l \otimes \boldsymbol{x}_k + b_l\right) \tag{12}$$

where $\otimes$ denotes the convolution operator [42], b_l is the bias in the lth group convolution kernel, and $f_{\text{conv}}(\cdot)$ is an activation function for the convolution layer.

The pooling layer is employed to compress the size of output feature maps from the convolution layer. Average pooling is conventional, and it achieves feature compression by calculating the average of elements in a pooling window [34]. The GAP layer applied to the proposed framework is different from local pooling in Fig. 10. It can calculate a representative average value by compressing the whole output feature map, as expressed by

$$o_l = \text{mean}\{\boldsymbol{z}_l\} = \frac{1}{h_p s_p} \sum_{m=1}^{h_p} \sum_{n=1}^{s_p} z_{k,j} \tag{13}$$

where $h_p \times s_p$ matches the feature map size processed by the GAP layer.

In Fig. 7, the GAP layer connects directly to the *Softmax* layer without adjusting the feature map size. Compared with a fully connected layer employed in a conventional CNN, the GAP layer has better performance [43]. Since no parameter optimization is attempted, the GAP layer reduces the quantity of data needed for parameter training and reduces the risk of neural-network overfitting. In addition, the GAP layer has low computational complexity and, therefore, accelerates network data processing compared with prior approaches. This is helpful for potential online diagnosis. After the pooling operation, there are g arrays corresponding to target categories of a $T^2$3L inverter.

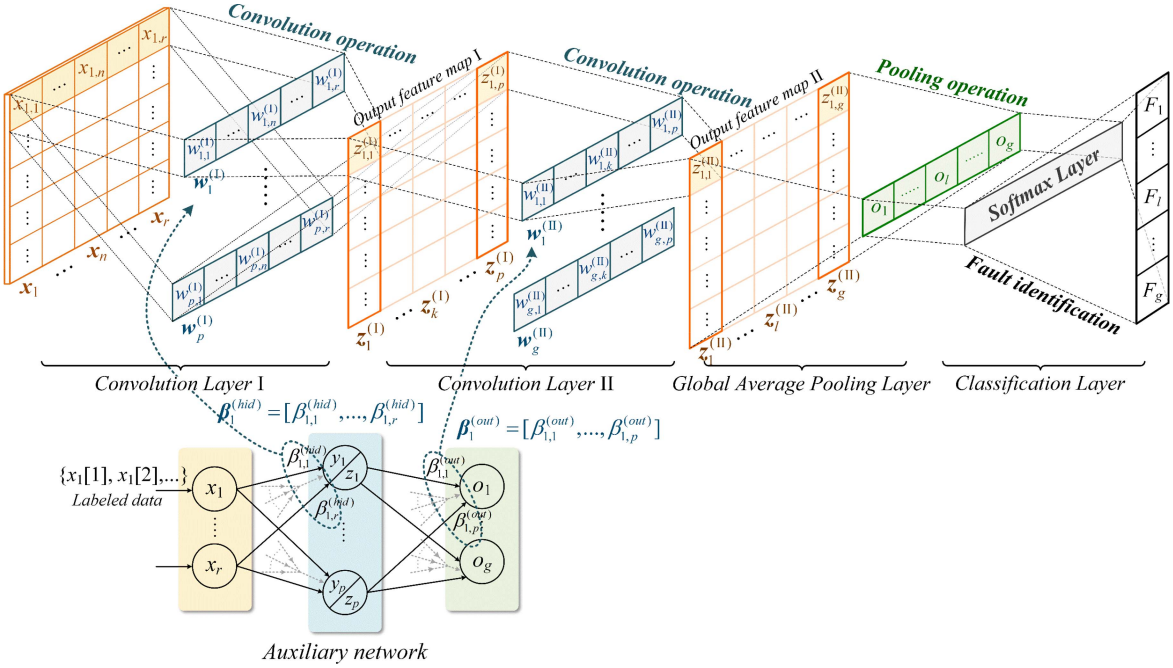

Fig. 7. Proposed data-driven diagnosis framework.

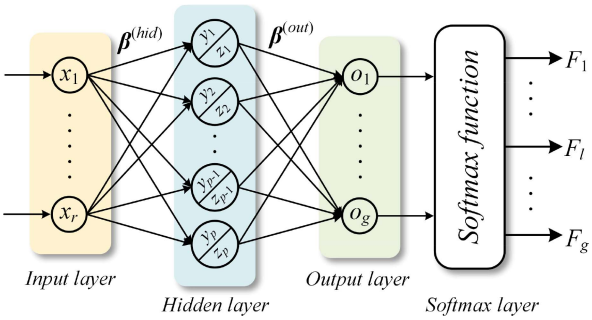

Fig. 8. Auxiliary neural-network structure.

The *Softmax* layer delivers a g-dimensional vector $\boldsymbol{F}$, in which elements F_l represent the probability that the input dataset x falls into category l.

B. Proposed Diagnosis Framework Sharing Filter Parameters

By comparing (10) and (11) with (12), it can be seen that the forward calculation data processes in CNNs and ANNs are similar. The trained parameters from a BPNN can be shared with a CNN to help discriminate data features. Considering that the given data are processed by the CNN in the form of 2-D maps, this parameter sharing requires a specific rearrangement of map weights from 1-D channels of the BPNN into convolution kernels of the CNN.

Following (10), weights between input and hidden layers of the BPNN form a $p \times r$ matrix $\beta^{(\mathrm{hid})}$ in which each row denotes a weight vector $\boldsymbol{\beta}_j^{(\mathrm{hid})}$ of hidden layer neuron j. Here, r is the input layer size and p is the hidden layer size. The data sequence received by each input neuron can be regarded as a channel ($\boldsymbol{x}_n$) of the input feature map ($\boldsymbol{X}$). Each neuron of the hidden layer

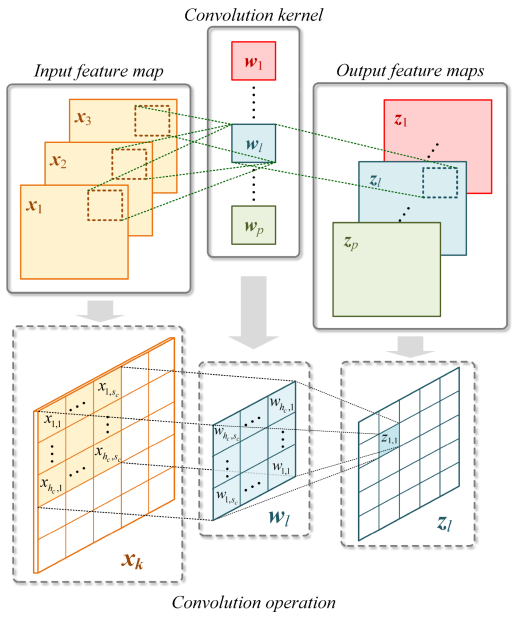

Fig. 9. Diagram of convolution layer operation.

delivers a new data channel ($\boldsymbol{z}_j$), and these p data channels form a new feature map. Ignoring the role of the activation function, the new feature map obtained by the hidden layers can be expressed as

$$\boldsymbol{Z} = \beta^{(\mathrm{hid})} \cdot \boldsymbol{X} + \boldsymbol{a} = \begin{bmatrix} \boldsymbol{z}_1 \\ \vdots \\ \boldsymbol{z}_j \\ \vdots \\ \boldsymbol{z}_p \end{bmatrix}$$

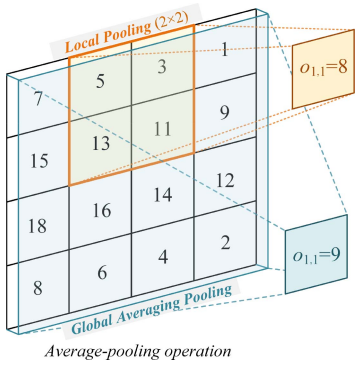

Fig. 10. Diagram of pooling layer operation.

$$= \begin{bmatrix} \beta_{1,1}^{(\text{hid})} & \cdots & \beta_{1,n}^{(\text{hid})} & \cdots & \beta_{1,r}^{(\text{hid})} \\ \vdots & \ddots & & & \vdots \\ \beta_{j,1}^{(\text{hid})} & & \beta_{j,n}^{(\text{hid})} & & \vdots \\ \vdots & & & \ddots & \vdots \\ \beta_{p,1}^{(\text{hid})} & \cdots & \cdots & \cdots & \beta_{p,r}^{(\text{hid})} \end{bmatrix} \cdot \begin{bmatrix} \boldsymbol{x}_1 \\ \vdots \\ \boldsymbol{x}_n \\ \vdots \\ \boldsymbol{x}_r \end{bmatrix} + \begin{bmatrix} a_1 \\ \vdots \\ a_j \\ \vdots \\ a_p \end{bmatrix}. \tag{14}$$

Similarly, a $g \times p$ matrix $\beta^{(\text{hid})}$ represents the output layer weights, with row vectors $\boldsymbol{\beta}_l^{\text{out}}$ that deliver a new output data channel. Based on (11), the output data matrix can be represented as

$$\boldsymbol{O} = \boldsymbol{\beta}^{(\text{out})} \cdot \boldsymbol{Z} + \boldsymbol{b} = \begin{bmatrix} \boldsymbol{o}_1 \\ \vdots \\ \boldsymbol{o}_l \\ \vdots \\ \boldsymbol{o}_g \end{bmatrix}$$

$$= \begin{bmatrix} \beta_{1,1}^{(\text{out})} & \cdots & \beta_{1,k}^{(\text{out})} & \cdots & \beta_{1,p}^{(\text{out})} \\ \vdots & \ddots & & & \vdots \\ \beta_{l,1}^{(\text{out})} & & \beta_{l,k}^{(\text{out})} & & \vdots \\ \vdots & & & \ddots & \vdots \\ \beta_{g,1}^{(\text{out})} & \cdots & \cdots & \cdots & \beta_{g,p}^{(\text{out})} \end{bmatrix} \cdot \begin{bmatrix} \boldsymbol{z}_1 \\ \vdots \\ \boldsymbol{z}_k \\ \vdots \\ \boldsymbol{z}_p \end{bmatrix} + \begin{bmatrix} b_1 \\ \vdots \\ b_l \\ \vdots \\ b_g \end{bmatrix}. \tag{15}$$

Weights $\boldsymbol{\beta}_j^{(\text{out})}$ and $\boldsymbol{\beta}_l^{(\text{out})}$ can also be applied to a CNN instead of convolution kernels to extract and classify feature information.

As shown in Fig. 7, a BPNN serves as an auxiliary neural network to learn circuit operating characteristics by training. The trained filter parameters applied to convolution kernels of the MCFC, in turn, provide feature discrimination capability. To share parameters developed by the BPNN, the sizes of convolution kernels ($\boldsymbol{w}^{(\text{I})}$, $\boldsymbol{w}^{(\text{II})}$) should match those of the input and hidden layers ($\beta^{(\text{hid})}$, $\beta^{(\text{out})}$), respectively. The convolution kernels also employ biases ($\boldsymbol{a}$, $\boldsymbol{b}$) and activation functions from the BPNN. In Fig. 7, parameter relationships among weight

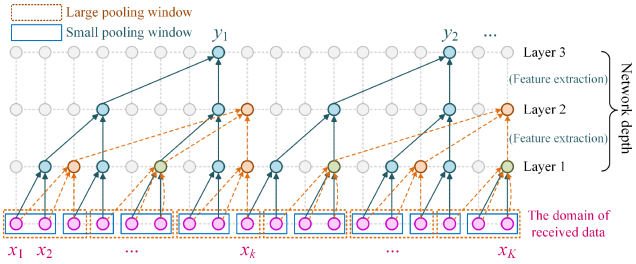

Fig. 11. Layer depth and receptive field.

vectors and convolution kernels are

$$\boldsymbol{w}_j^{(\text{I})} \otimes \boldsymbol{X} = \boldsymbol{\beta}_j^{(\text{hid})} \cdot \boldsymbol{X} \quad \left(w_{j,n}^{(\text{I})} = \beta_{j,r-n+1}^{(\text{hid})}\right) \tag{16}$$

$$\boldsymbol{w}_l^{(\text{II})} \otimes \boldsymbol{X} = \boldsymbol{\beta}_l^{(\text{out})} \cdot \boldsymbol{X} \quad \left(w_{l,k}^{(\text{II})} = \beta_{l,p-k+1}^{(\text{out})}\right) \tag{17}$$

where $w_{j,n}^{(\text{I})} \in \boldsymbol{w}_j^{(\text{I})}$ and $\beta_{j,r-n+1}^{(\text{hid})} \in \beta_j^{(\text{hid})}$; $w_{l,k}^{(\text{II})} \in \boldsymbol{w}_l^{(\text{II})}$ and $\beta_{l,p-n+1}^{(\text{out})} \in \boldsymbol{\beta}_l^{(\text{out})}$. A feature map consisting of 1-D arrays $\boldsymbol{z}_k^{(\text{II})}$ represents the output from convolution layer II and is fed into the GAP layer.

Based on this discussion, the proposed MCFC structure has the inherent merits of conventional CNNs, but with a simpler architecture. This reduces computational complexity and accelerates diagnosis. Fault identification capabilities of the MCFC are enhanced by auxiliary neural-network training and by providing appropriate weight parameters for convolution filters.

IV. Feature Map Construction and Parameter Setting

To use the MCFC to extract operating characteristics, sampled data sequences from all three phases are first transformed into 2-D feature maps. An MSSR method is proposed to form these maps from sampled time-series signals. The diagnosis strategy implemented to identify abnormal inverter operating modes is also illustrated in this section.

Changes in postfault ac currents are related to the moment at which a fault occurs. It may be difficult to determine faulty devices in an inverter based on transient variation of ac outputs. More information must be inferred from measured time-series data to ensure the accurate fault diagnosis. In a conventional CNN, sequential convolution layers and pooling layers extract data features. Network depth can be increased to help the system discriminate a wider range of distinct features in the input data: a larger *receptive field* for the system. The receptive field can also be expanded by increasing the size of convolution kernels or pooling windows. However, calculation effort increases as the network deepens, and an overlarge pooling window is likely to attenuate some feature information. Fig. 11 shows the relationship between the receptive field and the CNN structure, in which the input is a 1-D time-series sequence.

To expand the receptive field with limited network depth, an image construction method based on MSSR is applied to integrate 1-D three-phase current signals into a 2-D feature map. In this method, a moving detection window of fixed length is defined to collect sampled current data from each phase.

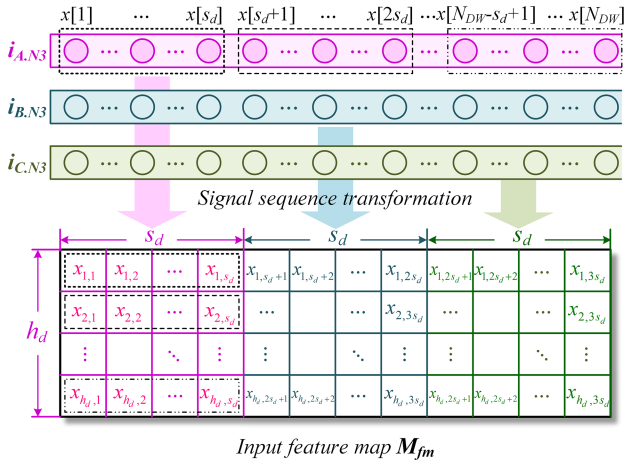

Fig. 12. Feature map construction based on MSSR.

Correspondingly, diagnosis signals can be represented by a $1 \times N_{\mathrm{DW}}$ array $\{i_{X.N3}[1], \ldots, i_{X.N3}[n], \ldots, i_{X.N3}[N_{DW}]\}$, covering N_{DW} samples. The input feature map ($\boldsymbol{M_{fm}}$) can be formed by rearranging the diagnosis signal array from each phase into a 2-D matrix. The proposed mapping is

$$\begin{cases} x_{k,l} = i_{A.N3}[(k-1)s_d + l] \\ x_{k,l+s_d} = i_{B.N3}[(k-1)s_d + l] \\ x_{k,l+2s_d} = i_{C.N3}[(k-1)s_d + l] \end{cases} \tag{18}$$

where $k = 1 : h_d, l = 1 : s_d$, and $x_{k,l}$ denotes the data at position (k, l) of $\boldsymbol{M_{fm}}$. Fig. 12 shows the conversion between the feature map $\boldsymbol{M_{fm}}$ and three-phase signal arrays $\boldsymbol{i_{X.N3}}$.

By applying the MSSR method, the size of the feature map is $h_f \times s_f$, with $h_f = h_d$ and $s_f = 3s_d$. The map can be used to evaluate operating conditions for each phase during a given interval $N_{\mathrm{DW}}T_s$, where T_s is the sampling period. The row dimension of $\boldsymbol{M_{fm}}$ should match the auxiliary neural-network input layer size, so $s_f = r$. More input neurons can extend the data dimension and enhance nonlinear fitting capability. A larger column vector (h_f) can capture more data in each channel of $\boldsymbol{M_{fm}}$, but this prolongs the system observation time. A longer detection window can also reduce the effects of signal noise or overshoot. A larger receptive field supports better discrimination among faults, although this requires more samples and time to observe the system's operating status. Since fast response is a crucial objective of the diagnosis strategy here, the size of the input feature map trades off data processing time and diagnostic accuracy. Through testing and comparison, the length of the detection window (N_{DW}) was set here to 16.

Fig. 13 shows the proposed overall fault diagnosis strategy based on the MCFC framework. For offline diagnosis, a signal array is formed for each phase for normal and fault scenarios that follow (18). The three-phase diagnosis arrays will be rearranged in the form of a 2-D map, where each column vector corresponds to an input channel of the auxiliary neural network. With samples of $i_{A.N3}$, $i_{B.N3}$, and $i_{C.N3}$, the input signal $i_{X.N3}[n]$ for each

TABLE I
HYPERPARAMETERS OF THE MCFC FRAMEWORK

Layer type	Kernel size, number	Input size	Output size
Detec. window	——	1×16, 3	1×16, 3
Conv. layer I	1×12, 12	4×12	4×12
Conv. layer II	1×12, 5	4×12	4×5
GAP layer	——	4×5	1×5
Softmax layer	——	1×5	1×5
Auxiliary network	——	12	5

Note: Detec. window refers to the detection window; and Conv. layer denotes the convolution layer.

channel $\boldsymbol{x}_{1,2,\ldots,r}$ can be expressed as

$$\begin{bmatrix} \mathbf{x}_{1+js_d} \\ \vdots \\ \mathbf{x}_{k+js_d} \\ \vdots \end{bmatrix} = \begin{bmatrix} i_{X.N3}[(n-1)s_d + 1] \\ \vdots \\ i_{X.N3}[(n-1)s_d + k] \\ \vdots \end{bmatrix} \tag{19}$$

where $k = 1 : s_d$, and $j = 0, 1, 2$ corresponds to $X = A, B, C$.

These 2-D data maps help the auxiliary neural network learn the operating characteristics of T^{2}3L inverters and adapt weight parameters under normal and fault conditions. The results lead to convolution kernel parameters from (16) and (17). During system operation, 1-D time-series data segments with 16 samples are collected from each phase and processed as in (7)–(9). Data segments from all three phases are transformed into input feature maps based on the MSSR method. Operating characteristics from each phase can be extracted by convolution kernels $(\boldsymbol{w}_X^{(\mathrm{I})}, \boldsymbol{w}_X^{(\mathrm{II})}, \boldsymbol{a}_X, \boldsymbol{b}_X)$. The MCFC applied to phase X can provide a target category label $\boldsymbol{F_X} = (F_{X0}, \ldots, F_{Xk}, \ldots, F_{Xg-1})$ through the *Softmax* layer, and fault indication signals F_{TXk} are prepared to indicate the status of transistors T_{Xk} following the classification results, as

$$\begin{cases} F_{TXk} = 1 & F_{Xk} = \max(F_{X0}, \ldots, F_{Xk}, \ldots, F_{Xg-1}) \\ F_{TXk} = F_{Xk} & F_{Xk} \neq \max(F_{X0}, \ldots, F_{Xk}, \ldots, F_{Xg-1}) \end{cases} \tag{20}$$

where F_{TX0} denotes the normal operation.

Based on Fig. 7, detailed predetermined parameters of the MCFC and auxiliary neural network are presented in Table I. The size of feature maps here is $s_{fm} = 12$ and $h_{fm} = 4$. To provide filter parameters, the auxiliary neural-network input layer has $r = s_{fm} = 12$. The size of the output layer in the auxiliary neural network is $g = 5$, referring to normal and fault states in individual transistors F_{X0}–F_{X4}. Phase X is normal if the value of F_{X0} is the maximum, T_{X1} has an OC fault if $F_{TX1} = 1$, and so on, following (20). To obtain the size of the hidden layer, empirical formulae from [44] and [45] can be applied to give a range, such as $p = \sqrt{r+g} + a,\ a \in [1, 10]$. From these, $p = 12$ was determined by testing various values of a. Note that an MCFC is employed for diagnosis of an individual phase. Filter parameters from the auxiliary neural network may differ for each phase. Training will need to probe each phase and learn its operating characteristics. On this basis, three MCFCs

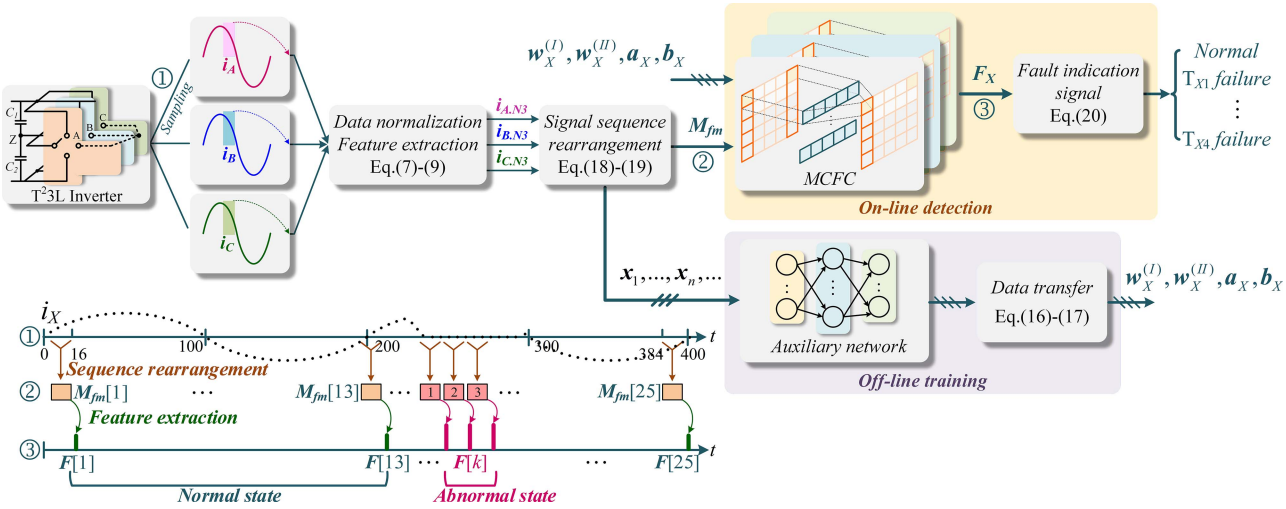

Fig. 13. Diagram of the proposed fault diagnosis strategy.

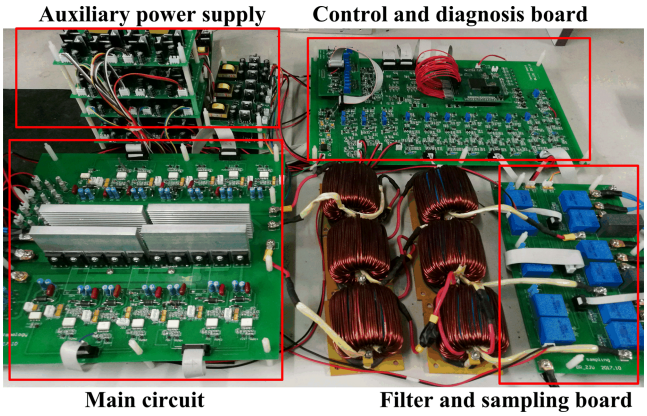

Fig. 14. Experimental inverter platform.

TABLE II
EXPERIMENTAL PLATFORM SPECIFICATIONS

Parameters	Symbols	Values
Input dc-link voltage	V_{dc}	400 V
Filter inductances	L_A, L_B, L_C	4 mH
Filter capacitors	C_A, C_B, C_C	4.7 μF
Switching frequency	f_s	10 kHz
Sampling period	T_s	100 μs
Rated power	P_r	1.5 kW

are employed to identify transistor OC faults in corresponding phases during T²3L inverter operation.

V. EXPERIMENTAL RESULTS

Experiments have been performed employing the T²3L inverter platform, as shown in Fig. 14, with specifications, as listed in Table II. A DSP (TMS320F28335) implements system control and diagnostic processes. The three-phase voltage and current waveforms are captured from an oscilloscope. The diagnosis current signals and the MCFC outputs are calculated and collected from the DSP. Fault diagnosis waveforms are plotted with MATLAB. A transistor OC fault can be simulated by disabling the corresponding gate driver.

A. Evaluation of MCFC Performance

Filter parameter training based on the auxiliary neural network is achieved with the neural-network pattern recognition (NNPR) application in MATLAB. The activation function $f_{\text{conv1}}(\cdot)$ of convolution layer I is the tanh function, and $f_{\text{conv2}}(\cdot)$ of convolution layer II is a linear function.

In the experiment, three-phase currents were measured with current sensors during normal or OC-fault-affected half cycles to generate training samples. Current signals were sampled at the switching frequency, 10 kHz, and each detection window collected current signals for 1.6 ms. For each operating condition, 800 labeled samples were collected from at least eight half cycles. Since data were processed in sets of 16 points, 800 samples form 50 feature maps with 50 different starting points. The total number of training samples was 10 400 and included cases with normal operation and with 13 distinct single-transistor fault operation modes.

Based on the topological symmetry of a three-phase T²3L inverter, let us consider the MCFC applied to phase A fault diagnosis as an example. Training set classification was carried out in other neural-network-based models, including different combinations of BNPP, MCFC, and current signals $i_{X.N}$ and $i_{X,N3}$, as listed in Table III. Network parameters were optimized by training the BPNN and the MCFC auxiliary neural network in the NNPR application of MATLAB to obtain diagnostic percentages for comparison in Table III. BPNN-2 has the same structure as the auxiliary neural network. BPNN-1 is different, with only one channel in its input layer corresponding to signals from each phase current, and $r = 3$. The sizes of the other layers were held constant ($p = 12$ and $g = 5$). As in [46], classification metrics termed *precision rate* (*PRE*) and *recall rate* (*REC*) can

TABLE III
EVALUATION RESULTS OF VARIOUS MODELS

Model		Model I $i_{X,N3}$ + BPNN-1		Model II $i_{X,N}$ + BPNN-2		Model III $i_{X,N3}$ + BPNN-2		Model IV $i_{X,N}$ + MCFC		Model V $i_{X,N3}$ + MCFC	
Performance		*PRE* (%)	*REC* (%)	*PRE* (%)	*REC* (%)	*PRE* (%)	*REC* (%)	*PRE* (%)	*REC* (%)	*PRE* (%)	*REC* (%)
0	Normal	92.4	92.9	93.7	96.0	97.5	98.7	97.6	99.1	100.0	100.0
1	T_{A1} OCF	60.5	69.0	96.5	96.0	95.9	92.5	100.0	100.0	96.2	100.0
2	T_{A2} OCF	62.0	59.5	67.1	51.0	93.1	94.0	92.7	76.0	100.0	100.0
3	T_{A3} OCF	83.3	70.0	81.2	80.0	94.0	86.5	96.1	98.0	100.0	96.0
4	T_{A4} OCF	75.7	76.5	89.9	93.5	94.0	93.5	96.1	98.0	100.0	100.0
Average		85.5	85.5	91.1	91.1	96.5	96.5	97.2	97.2	99.7	99.7

be adopted to evaluate the overall detection performance. They are expressed as

$$\begin{cases} \mathrm{PRE} = \frac{\mathrm{TP}}{\mathrm{TP+FP}} \\ \mathrm{REC} = \frac{\mathrm{TP}}{\mathrm{TP+FN}}. \end{cases} \tag{21}$$

In Table III, if an OC fault F_{TX1} actually occurs, TP (true positive) refers to the number of correct fault category predictions into F_{TX1}, FP is the number of false positives classified into this fault category, and FN (false negative) refers to the number of instances incorrectly predicted as other operating conditions (F_{TXk}, $k \neq 1$). Thus, PRE is the ratio of correctly classified instances to all instances identified under this condition, and REC denotes the ratio of correctly classified instances to all instances belonging to a specific operating condition.

As shown in Table III, the feature extraction capability of the BPNN alone was limited due to its shallow structure and small receptive field. The diagnostic precision of the proposed MCFC framework (Model IV and Model V) was better than for a conventional BPNN model. In Model II and Model IV, PRE and REC were relatively low when faults occur in middle transistors since current signal features for these faults are similar initially to normal operation and to half-bridge transistor fault scenarios. Decay components extracted by (9) improved classification precision in Model III and Model V. Comparing Model I with Model III, the MSSR method offered a higher classification precision rate and higher recall rate since Model II can receive more data to enhance its learning capability by extending the dimension of input samples. Model V had superior performance, with an average classification precision rate of 99.7% for this training set.

To display the classification performance of the proposed MCFC framework (Model V), a multiclass confusion matrix [41] was applied, as shown in Fig. 15. The ordinate axis of the multiclass confusion matrix represents the category label output from Model V. The abscissa axis represents the actual category label. The diagonal cells denote the number of samples in each category, and other cells contain the number of incorrectly distinguished samples. In Fig. 15, the proportion of diagonal data in the matrix to the total data of each row and column can be represented by PRE and REC, respectively, to show OC-fault diagnosis accuracy for phase A. Model V was not perfect in this test, as two cases were missed out of 650 tests. The actual category label of the misdiagnosed sample groups was the T_{A3}

Fig. 15. Training results for model V in the form of a confusion matrix.

OC fault, but the MCFC reported a T_{A1} OC fault. The reason is that both T_{A1} and T_{A3} provide effective current paths during the positive half cycle, and these two faults cause positive current decay. Although diagnosis signals obtained by (9) can make the decay characteristics in various fault scenarios more distinct, features extracted by the MCFC from some detection windows may still be similar under T_{A1} and T_{A3} OC-fault conditions.

To analyze the possibility of misdiagnosis under various situations, define MPS and MNS as

$$\begin{cases} MPS = 1 - SPE = \frac{\mathrm{FP}}{\mathrm{TN+FP}} \\ MNS = 1 - \mathrm{REC} = \frac{\mathrm{FN}}{\mathrm{TP+FN}} \end{cases} \tag{22}$$

where TN (true negative) represents, for a specific operating condition, the number of instances correctly predicted as other conditions, and SPE is the specificity rate, which represents the ratio of samples correctly classified into other operating conditions. Following (22), the misdiagnosis possibility of T_{A1} failure in these tests was MPS = 0.003 and MNS = 0. These indicate that the probability of normal or T_{A2}–T_{A4} fault modes being misdiagnosed as a T_{A1} fault was 0.003, and the probability of a T_{A1} fault being misdiagnosed as other categories was 0. Similarly, the misdiagnosis probability under a T_{A3} fault condition was MPS = 0 and MNS = 0.04. As intended, the

TABLE IV
EFFECTS OF HARMONIC DISTORTION ON DIAGNOSIS RESULTS

Injected third and fifth harmonic component	THD of i_A	Diagnosis accuracy (%)
0	1.98%	99.7%
1%	2.54%	99.1%
2%	3.61%	98.5%
4%	6.20%	97.2%
6%	8.94%	96.3%
8%	11.73%	95.2%

proposed method has high diagnostic reliability. There were no false positives during normal operation.

The diagnostic accuracy of Model V under various current harmonic conditions should be considered. In this test, the third and fifth harmonic components were injected into phase currents during system operation to test the performance of the proposed method. Table IV lists the results, which show that the current harmonics degrade diagnosis accuracy slightly. Harmonic signals change decay features in postfault three-phase currents and introduce some uncertainty, so fault identification of transistors that are enabled for one half cycle, such as T_{A1} and T_{A3}, will be more challenging. In this scenario, the proposed method achieves diagnosis accuracy above 95% even when the current THD reaches almost 12%.

Nonlinear loads, such as the uncontrolled rectifier loads, could have a similar impact. The performance of Model V was tested with an uncontrolled rectifier load, with currents shown in Fig. 16(a). The decay of $i'_{A.N}$ differs from $i_{A.N}$ due to harmonic components. In this circumstance, the diagnosis accuracy decreased to 86.6%. The diagnostic results for phase A are presented in Fig. 16(b). The left column there shows that false positives can occur during normal operation because of load waveform details. False negatives (the top row) are much less likely but occurred in two tests during T_{A3} faults. Enhanced training scenarios or longer detection windows are likely to be of benefit for nonlinear loads and harmonics. Future work will focus on improving the diagnosis accuracy of this approach under various types of loads and the influence of harmonics.

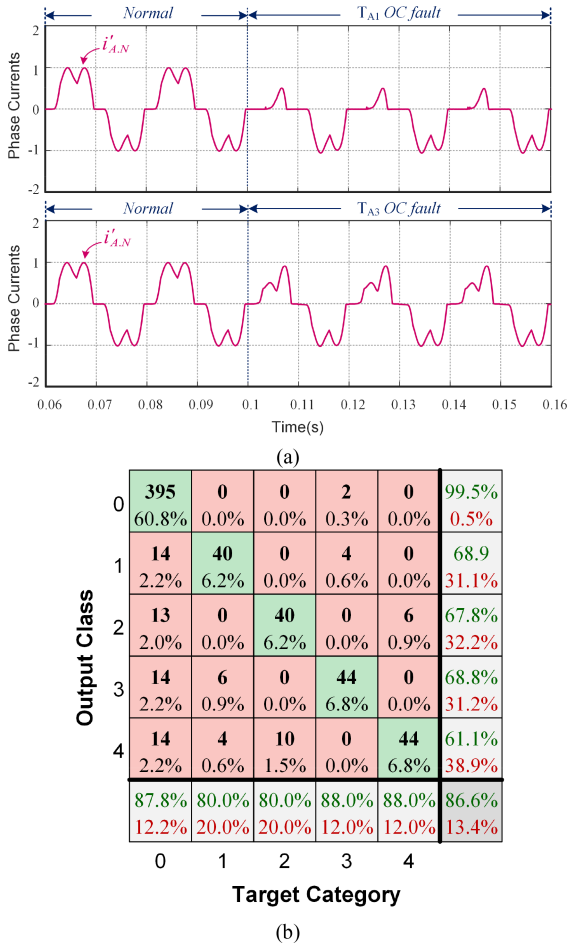

Fig. 16. Effects of uncontrolled rectifier loads on diagnostic results. (a) Current of phase A due to T_{A1} or T_{A3} failure. (b) Diagnostic results of phase A in the form of a confusion matrix.

B. Analysis of Fault Diagnosis Results

Fig. 17 shows real-time diagnosis results for phase A of the tested T^{2}3L inverter with the MCFC active. The MCFC provides fault indication signals (F_{normal}, F_{TA1}–F_{TA4}) corresponding to normal operation and to various OC-fault scenarios. Each point in F_{TAj} represents a feature classification result from the MCFC for a feature map. In Fig. 17, a transistor OC fault will cause distortion in the positive or negative current half cycle. By extracting fault features from current data, the MCFC can detect abnormal operation, and F_{TAj} is triggered high to distinguish the faulty device.

To further analyze the feature extraction abilities of various data-driven models, a visualization method called *t-distributed stochastic neighbor embedding* (t-SNE) was used to visualize the output of each network layer under a test set by reducing the dimension of data samples from the original feature space into an easy-to-visualize map [39], [47]. For each operating scenario of phase A, three-phase current data were collected over 400 sampling cycles during a T^{2}3L inverter experiment, and 2000 samples out of the total, representing normal and single-fault scenarios of phase A, were used to form the test set. A t-SNE plot is an effective way to show relationships among data features of each layer in different neural networks in terms of their distributions on a given plane. Figs. 18–20 show the data feature distributions of each layer in Models III, IV, and V, respectively, based on t-SNE. Note that the axis values in Figs. 18–20 show the relative distance between data points, reflecting the similarity of corresponding features within the data. The actual numbers have no special meaning. Clustered points in each graph imply high similarity of data features. Points with the same color and shape in Figs. 18–20 belong to the same operating condition. The more tightly they cluster, the stronger and more accurate the feature extraction capability of the network.

Current diagnosis signals representing various scenarios (colors and shapes) fed into input layers are evenly distributed in Figs. 18(a), 19(a), and 20(a). However, there are still differences between the distributions of data features of $i_{X.N}$ and $i_{X.N3}$. It can be seen that the distribution of different data

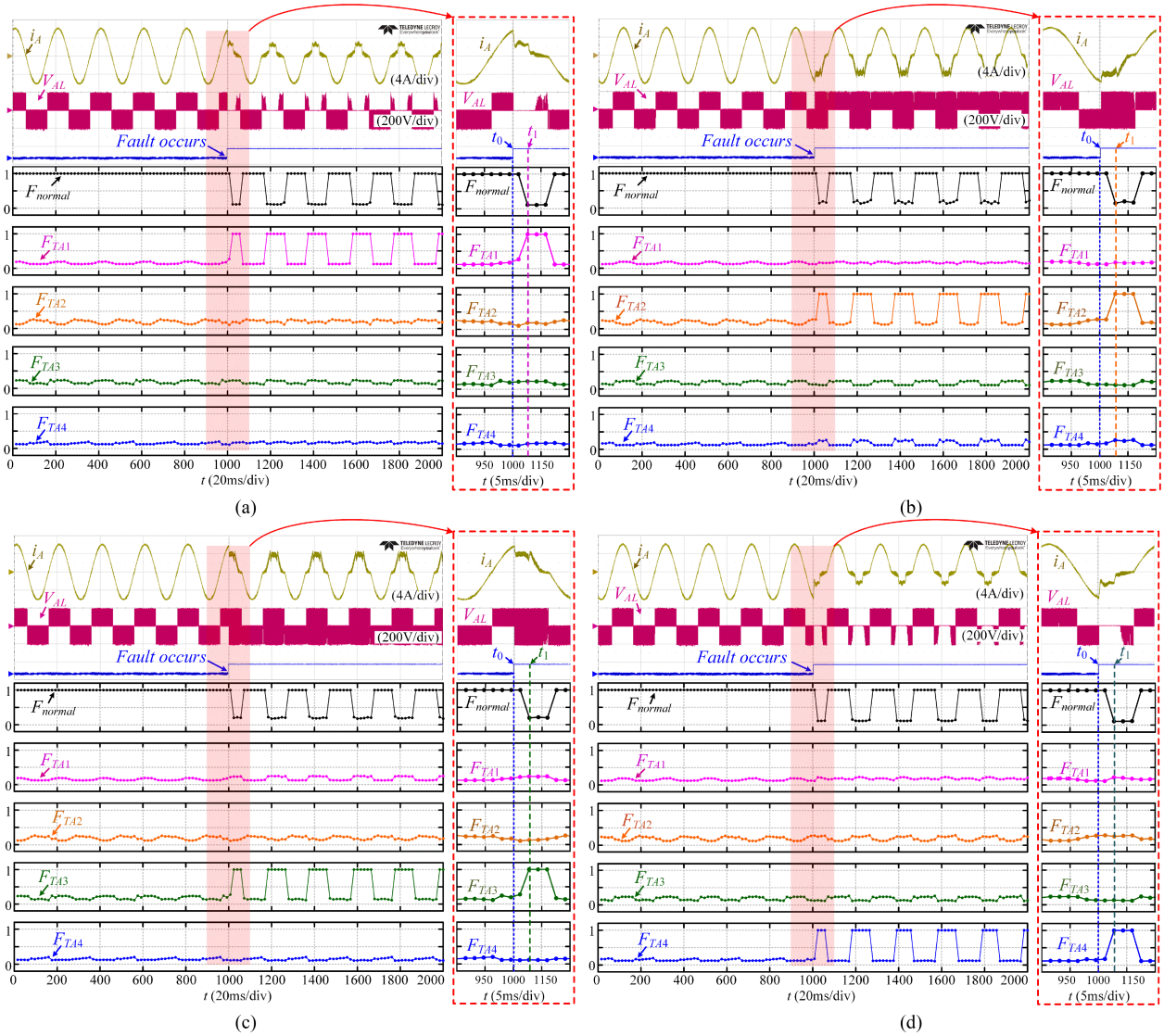

Fig. 17. Experimental waveforms of diagnosis results under (a) T_{A1} OC fault, (b) T_{A2} OC fault, (c) T_{A3} OC fault, and (d) T_{A4} OC fault.

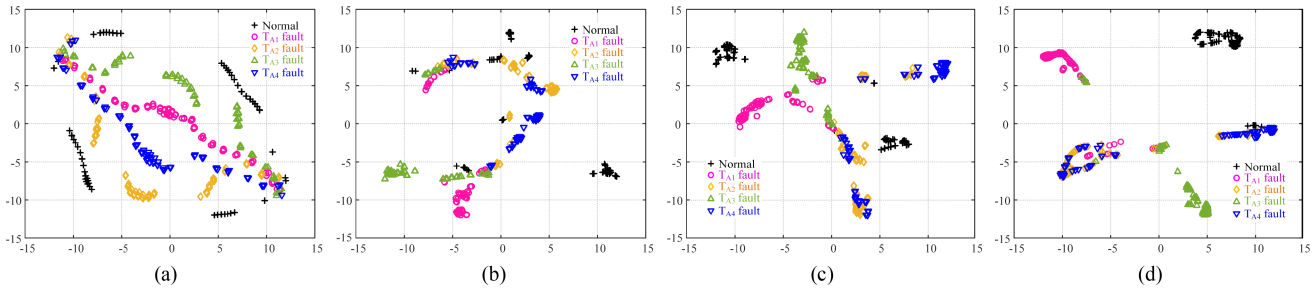

Fig. 18. Scatter plots of feature visualization based on BPNN-2 test data and $\boldsymbol{i_{A\_N3}}$ based on t-SEN. (a) Feature distribution of input data. (b) Feature distribution of hidden layer. (c) Feature distribution of output layer. (d) Feature distribution of classification layer.

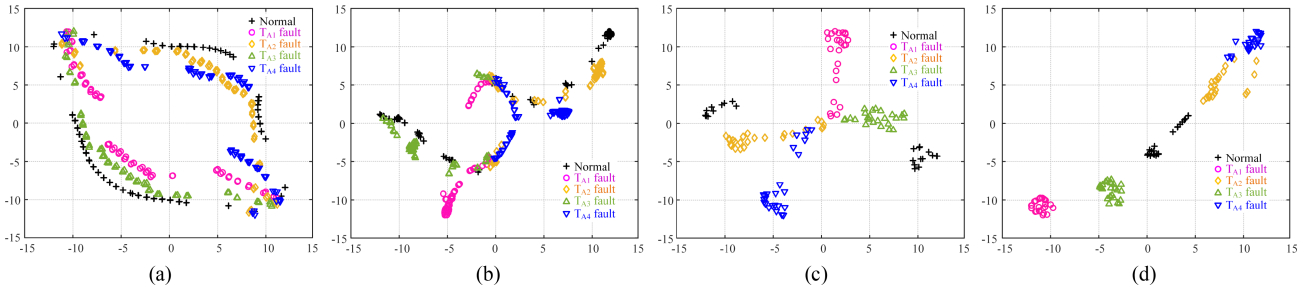

Fig. 19. Scatter plots of feature visualization based on MCFC test data and $i_{A.N}$ based on t-SEN. (a) Feature distribution of input data. (b) Feature distribution of convolution layer I. (c) Feature distribution of convolution layer II. (d) Feature distribution of classification layer.

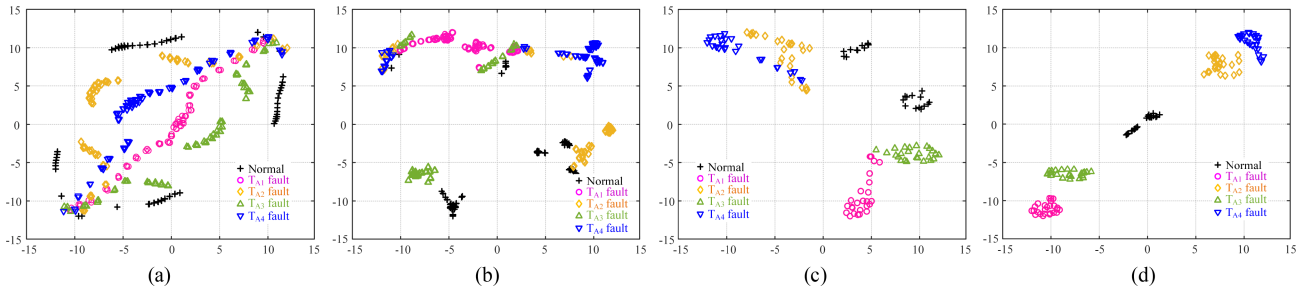

Fig. 20. Scatter plots of feature visualization based on MCFC test data and $i_{A.N3}$ based on t-SEN. (a) Feature distribution of input data. (b) Feature distribution of convolution layer I. (c) Feature distribution of convolution layer II. (d) Feature distribution of classification layer.

TABLE V
COMPARISON OF DIAGNOSIS METHODS

No.	Data-driven Method	Complexity	Diagnosed Inverters	Target categories	Diagnosis accuracy	Diagnosis time
(1)	MSDP+SSFA+ANN[26]	Low	Three-phase 2L inverter	10	≈100%	≈20 ms
(2)	WSCNN[37]	Medium	Three-phase 2L inverter	7	≈99.7%	≈58 ms
(3)	Structured ANN[27]	High	Three-phase 2L inverter	18	≈99.0%	≈20 ms
(4)	Circuit average model +ANN[28]	Low	Three-phase 2L inverter	7	≈100%	≈0.5 ms
(5)	ASLSTMN[32]	High	Three-phase NPC 3L inverter	19	≈99.3%	≈20 ms
(6)	CNN[36]	Medium	Three-phase ANPC 3L inverter	19	≈99.6%	≤20 ms
(7)	1-D CNN[38]	Low	Three-phase NPC 3L inverter	79	≈100%	≤20 ms
(8)	DRFN[33]	Medium	Three-phase T-type 3L inverter	27	≈99.2%	≈21 ms
(9)	Proposed method	Low	Three-phase T-type 3L inverter	13	≈99.7%	≈3.6 ms

points is denser and more difficult to distinguish in Fig. 18(a). Compared with $i_{X.N}$, the processed $i_{X.N3}$ can further highlight fault characteristics. As shown in Fig. 18(b)–(d), different operating conditions cannot be well clustered separately with these BPNN-2 parameters. In comparison, the feature extraction ability of the complete MCFC increases with the depth of the network since each feature can be clustered in Fig. 19(b)–(d). Fig. 20(d) is the key result here, indicating that the MCFC can classify various operation conditions distinctly by employing $i_{X.N3}$, and five separate clusters are formed by points mapped from output signals of the *Softmax* layer, corresponding to $g = 5$. This classification visualization helps to illustrate the effectiveness of the proposed fault diagnosis framework.

Experimental results under varying (linear) load conditions are given in Fig. 21 to verify the robustness of the proposed method. As shown in Fig. 21(a) and (b), misdiagnosis will not occur following an abrupt change from 50% load to 100% load since the influence of current amplitude variation was reduced by data normalization and the GAP layer.

Fig. 22 shows detection response times for a T_{A1} OC fault, following the operating scenario of Fig. 17(a) with the fault imposed at various times. In Fig. 22(a), the diagnosis response when T_{A1} fails at various moments of a fundamental cycle is listed. The fault was triggered at 20 evenly spaced moments over a 50 Hz fundamental period (T_F), and the diagnosis time is represented as a percentage of T_F. Diagnosis time is relatively long when the phase current is negative since a T_{A1} OC fault will

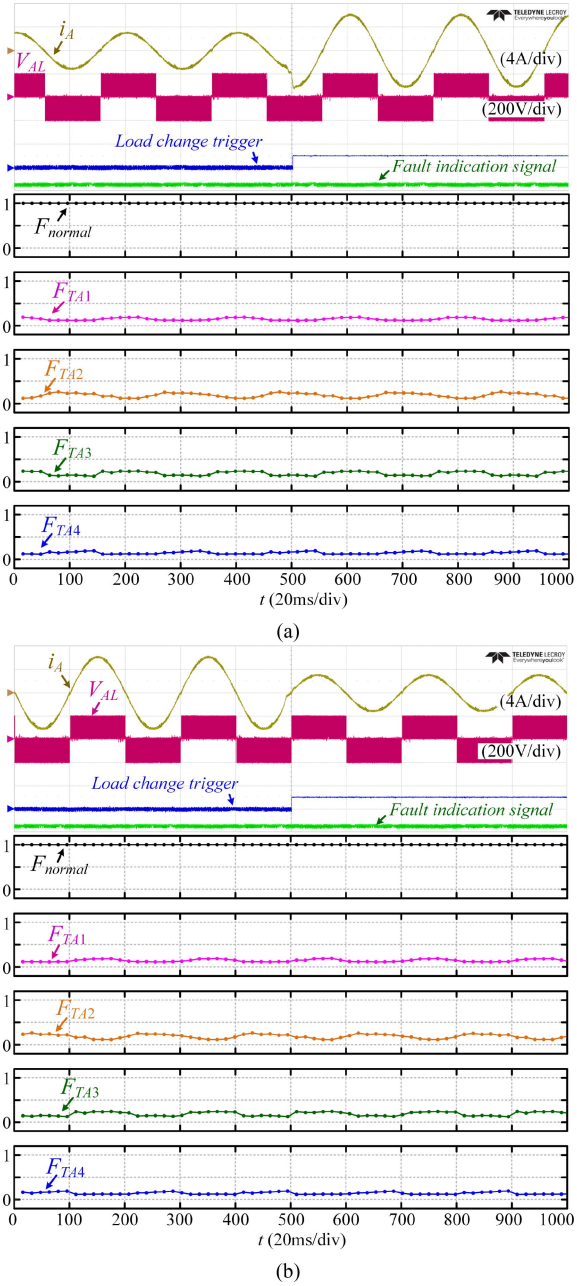

Fig. 21. Dynamic response with load changes. (a) From half load to full load. (b) From full load to half load.

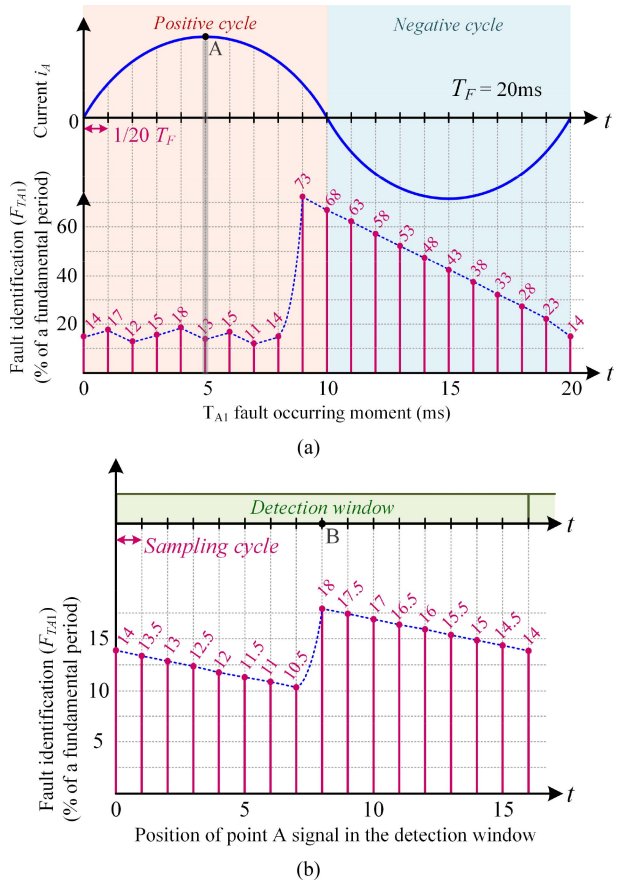

Fig. 22. Diagnosis response when a T_{A1} OC fault occurs at 20 evenly spaced moments. (a) In a fundamental period. (b) In a 16-sample detection window.

not affect system operation until $i_A > 0$. During positive phase current, fault detection takes about 3 ms. The maximum and minimum diagnosis times are 3.6 ms (18% of T_F) and 2.2 ms (11% of T_F), linked to the moment at which the fault occurs. Consider the case in which a T_{A1} OC fault occurs at the current peak, shown as point A in the figure. For this example case, the effect of fault time on diagnosis response also depends on when a T_{A1} fault occurs during the 16-sample detection window. The effect is shown in Fig. 22(b). The number of abnormal samples gathered will affect the fault identification results. For example, if point A happens to correspond to the ninth sample out of 16, the fact that the fault is preceded by eight normal samples slows the detection time to 18% of a fundamental period—samples will be needed from the subsequent detection window. Fault features can be extracted effectively from a set of 16 samples if more than half of the samples are abnormal. The timing is affected mostly by the abnormal data fraction in detected feature maps. Quick detection requires enhancing the learning capabilities of the auxiliary neural network by optimizing data processing and training. In future work, we seek to achieve this without additional network complexity.

VI. Comparisons of Diagnosis Methods

To compare the performance of the proposed method to prior work, Table V discusses the capabilities of several data-driven methods applied to inverter fault diagnosis. The complexity of listed methods is assigned based on the size and depth of neural networks, and on the number of parameters that must be set. The results imply that diagnosis time is related to the time window of collected input signals, the data preprocessing approach, and the complexity of the network.

Methods (1), from [26], and (2), from [37], can effectively identify multiple OC faults in two-level (2L) inverters with a simple neural network. They obtain fast test times for input diagnosis signals. Method (4), as reported in [28], has excellent performance and is based on an analytical inverter model. The

accurate model is essential. As the output voltage level increases, circuits transition to multilevel configurations, in which more abnormal operation categories will appear due to transistor OC faults. Multilevel inverters will require stronger diagnostic identification capability. To handle this issue, CNNs and ASLSTMN can be employed in 3L inverters. Method (5), from [32], and method (6), from [36], were able to distinguish OC faults in each transistor or clamp diode. A novel 1-D improved CNN in method (7), from [38], achieved 100% accuracy for a large number of fault modes with diagnosis time of just under one cycle. These methods are suitable for online diagnosis, although all but Li et al. [28] require essentially a full cycle of data. Method (8), from [33], uses a DRFN for $T^2$3L inverters. The algorithm can diagnose multiple OC faults, and the data calculation time is only 1 ms. However, the fault detection time is 21 ms because a full cycle of samples is needed.

The method proposed in this article needs only 16 current signal samples for each phase to form one input feature map. With a 0.1-ms sample interval, only 1.6 ms is needed to gather information. The time-series data in each detection window can be gathered quickly and the structure of the MCFC is relatively shallow. Compared with prior methods, the proposed method has a fast diagnosis response with high accuracy, trading off the capability to distinguish large numbers of fault categories. The method of [28] is challenging to adapt to $T^2$3L inverters since it is derived for a 2L circuit and requires the accurate analytic models. The MCFC approach uses training data rather than circuit models and should be more flexible than the approach in [28].

VII. Conclusion

A data-driven method is proposed in this article for T-type inverter OC-fault diagnosis based on an MCFC framework. A simple BPNN as a feature filter learns current characteristics to track system operating conditions. The MCFC extracts the degree of current distortion through a distortion amplifier and convolution operations, and classifies the system operating mode based on shared filter parameters. The output results of the MCFC can be obtained over a complete feature map by compressing extracted data in a GAP layer. A signal processing function is proposed to discriminate current distortion, and an MSSR strategy is presented to prepare input feature maps from sampled time-series data. The combined processes deliver high diagnostic accuracy, leading directly to fault identification. The diagnostic accuracy of the proposed convolution-pooling model can be as high as 99.7%, substantially higher than for a conventional BPNN approach. The method is robust and fast. In the experimental tests, fault features could be identified within about 15% of a fundamental period. The proposed method compares favorably with past work in terms of complexity, accuracy, training effort, and response time. Future efforts should be able to enhance immunity to waveform distortion as would be expected with nonlinear loads.

Acknowledgment

The Principal Supervisors were H. Ma and P. T. Krein.

References

[1] M. Schweizer and J. W. Kolar, "Design and implementation of a highly efficient three-level T-type converter for low-voltage applications," *IEEE Trans. Power Electron.*, vol. 28, no. 2, pp. 899–907, Feb. 2013.

[2] A. Anthon, Z. Zhang, M. A. E. Andersen, D. G. Holmes, B. McGrath, and C. A. Teixeira, "The benefits of SiC MOSFET in a T-type inverter for grid-tie applications," *IEEE Trans. Power Electron.*, vol. 32, no. 4, pp. 2808–2821, Apr. 2017.

[3] A. Sheir, M. Z. Youssef, and M. Orabi, "A novel bidirectional T-type multilevel inverter for electric vehicle applications," *IEEE Trans. Power Electron.*, vol. 34, no. 7, pp. 6648–6658, Jul. 2019.

[4] S. Yang, A. Bryant, P. Mawby, D. Xiang, L. Ran, and P. Tavner, "An industry-based survey of reliability in power electronic converters," *IEEE Trans. Ind. Appl.*, vol. 47, no. 3, pp. 1441–1451, May/Jun. 2011.

[5] F. Wu and J. Zhao, "A real-time multiple open-circuit fault diagnosis method in voltage-source-inverter fed vector controlled drives," *IEEE Trans. Power Electron.*, vol. 31, no. 2, pp. 1425–1437, Feb. 2016.

[6] U. Choi, J. Lee, F. Blaabjerg, and K. Lee, "Open-circuit fault diagnosis and fault-tolerant control for a grid-connected NPC inverter," *IEEE Trans. Power Electron.*, vol. 31, no. 10, pp. 7234–7247, Oct. 2016.

[7] H. Zhao and L. Cheng, "Open switch fault diagnostic method for back-to-back converters of doubly fed wind power generation system," *IEEE Trans. Power Electron.*, vol. 33, no. 4, pp. 3452–3461, Apr. 2018.

[8] X. Wang, Z. Wang, Z. Xu, J. He, and W. Zhao, "Diagnosis and tolerance of common electrical faults in T-type three-level inverters fed dual three-phase PMSM drives," *IEEE Trans. Power Electron.*, vol. 35, no. 2, pp. 1753–1769, Feb. 2020.

[9] Y. Liang, R. Wang, and B. Hu, "Single-switch open-circuit diagnosis method based on average voltage vector for three-level T-type inverter," *IEEE Trans. Power Electron.*, vol. 36, no. 1, pp. 911–921, Jan. 2021.

[10] B. Wang, Z. Li, Z. Bai, P. T. Krein, and H. Ma, "Real-time diagnosis of multiple transistor open-circuit faults in a T-type inverter based on finite-state machine model," *CPSS Trans. Power Electron. Appl.*, vol. 5, no. 1, pp. 79–90, Mar. 2020.

[11] C. Shu, C. Ya-Ting, Y. Tian-Jian, and W. Xun, "A novel diagnostic technique for open-circuited faults of inverters based on output line-to-line voltage model," *IEEE Trans. Ind. Electron.*, vol. 63, no. 7, pp. 4412–4421, Jul. 2016.

[12] S. Xu, J. Zhang, and J. Hang, "Investigation of a fault-tolerant three-level T-type inverter system," *IEEE Trans. Ind. Appl.*, vol. 53, no. 5, pp. 4613–4623, Sep./Oct. 2017.

[13] U. Choi, K. Lee, and F. Blaabjerg, "Diagnosis and tolerant strategy of an open-switch fault for T-type three-level inverter systems," *IEEE Trans. Ind. Appl.*, vol. 50, no. 1, pp. 495–508, Jan./Feb. 2014.

[14] B. Wang, Z. Li, Z. Bai, P. Krein, and H. Ma, "A voltage vector residual estimation method based on current path tacking for T-type inverter open-circuit fault diagnosis," *IEEE Trans. Power Electron.*, vol. 36, no. 12, pp. 13460–13477, Dec. 2021.

[15] X. Ge, J. Pu, B. Gou, and Y. Liu, "An open-circuit fault diagnosis approach for single-phase three-level neutral-point-clamped converters," *IEEE Trans. Power Electron.*, vol. 33, no. 3, pp. 2559–2570, Mar. 2018.

[16] T. Peng et al., "A uniform modeling method based on open-circuit faults analysis for NPC-three-level converter," *IEEE Trans. Circuits Syst. II, Express Briefs*, vol. 66, no. 3, pp. 457–461, Mar. 2019.

[17] S. S. Moosavi et al., "Artificial neural network-based fault diagnosis in the AC–DC converter of the power supply of series hybrid electric vehicle," *IET Electr. Syst. Transp.*, vol. 6, no. 2, pp. 96–106, Jun. 2016.

[18] L. Kou, C. Liu, G.-W. Cai, J.-N. Zhou, Q.-D. Yuan, and S.-M. Pang, "Fault diagnosis for open-circuit faults in NPC inverter based on knowledge-driven and data-driven approaches," *IET Power Electron.*, vol. 13, no. 6, pp. 1236–1245, May 2020.

[19] Y. Xia and Y. Xu, "A transferrable data-driven method for IGBT open-circuit fault diagnosis in three-phase inverters," *IEEE Trans. Power Electron.*, vol. 36, no. 12, pp. 13478–13488, Dec. 2021.

[20] A. Bernieri, M. D'Apuzzo, L. Sansone, and M. Savastano, "A neural network approach for identification and fault diagnosis on dynamic systems," *IEEE Trans. Instrum. Meas.*, vol. 43, no. 6, pp. 867–873, Dec. 1994.

[21] W. Wu, G. Feng, Z. Li, and Y. Xu, "Deterministic convergence of an online gradient method for BP neural networks," *IEEE Trans. Neural Netw.*, vol. 16, no. 3, pp. 533–540, May 2005.

[22] B. Cai, Y. Zhao, H. Liu, and M. Xie, "A data driven fault diagnosis methodology in three-phase inverters for PMSM drive systems," *IEEE Trans. Power Electron.*, vol. 32, no. 7, pp. 5590–5600, Jul. 2017.

[23] I. Abari, A. Lahouar, M. Hamouda, J. B. H. Slama, and K. Al-Haddad, "Fault detection methods for three-level NPC inverter based on DC-bus electromagnetic signatures," *IEEE Trans. Ind. Electron.*, vol. 65, no. 7, pp. 5224–5236, Jul. 2018.
[24] Z. Wang, Z. Huang, C. Song, and H. Zhang, "Multiscale adaptive fault diagnosis based on signal symmetry reconstitution preprocessing for microgrid inverter under changing load condition," *IEEE Trans. Smart Grid*, vol. 9, no. 2, pp. 797–806, Mar. 2018.
[25] P. Han, X. He, H. Ren, and Y. Wang, "Fault diagnosis and system reconfiguration strategy of a single-phase three-level neutral-point-clamped cascaded inverter," *IEEE Trans. Ind. Appl.*, vol. 55, no. 4, pp. 3863–3876, Jul./Aug. 2019.
[26] Z. Huang, Z. Wang, and H. Zhang, "Multiple open-circuit fault diagnosis based on multistate data processing and subsection fluctuation analysis for photovoltaic inverter," *IEEE Trans. Instrum. Meas.*, vol. 67, no. 3, pp. 516–526, Mar. 2018.
[27] M. A. Masrur, Z. Chen, and Y. Murphey, "Intelligent diagnosis of open and short circuit faults in electric drive inverters for real-time applications," *IET Power Electron.*, vol. 3, no. 2, pp. 279–291, Mar. 2010.
[28] Z. Li, Y. Gao, X. Zhang, B. Wang, and H. Ma, "A model-data-hybrid-driven diagnosis method for open-switch faults in power converters," *IEEE Trans. Power Electron.*, vol. 36, no. 5, pp. 4965–4970, May 2021.
[29] Q. Sun, Y. Wang, and Y. Jiang, "A novel fault diagnostic approach for DC-DC converters based on CSA-DBN," *IEEE Access*, vol. 6, pp. 6273–6285, 2018.
[30] M. Baker, H. Althuwaini, and M. B. Shadmand, "Artificial intelligence based anomaly detection and classification for grid-interactive cascaded multilevel inverters," in *Proc. 3rd Int. Conf. Smart Grid Renewable Energy*, Mar. 2022, pp. 1–6.
[31] M. Zhao, S. Zhong, X. Fu, B. Tang, S. Dong, and M. Pecht, "Deep residual networks with adaptively parametric rectifier linear units for fault diagnosis," *IEEE Trans. Ind. Electron.*, vol. 68, no. 3, pp. 2587–2597, Mar. 2021.
[32] Y. Si, R. Wang, S. Zhang, W. Zhou, A. Lin, and Y. Wang, "Fault diagnosis based on attention collaborative LSTM networks for NPC three-level inverters," *IEEE Trans. Instrum. Meas.*, vol. 71, Apr. 2022, Art. no. 3512416.
[33] Z. Xing, Y. He, and W. Zhang, "An online multiple open-switch fault diagnosis method for T-type three-level inverters based on multimodal deep residual filter network," *IEEE Trans. Ind. Electron.*, vol. 70, no. 10, pp. 10669–10679, Oct. 2023.
[34] W. Gong et al., "A novel deep learning method for intelligent fault diagnosis of rotating machinery based on improved CNN-SVM and multichannel data fusion," *Sensors*, vol. 19, 2019, Art. no. 1693.
[35] S. Kiranyaz, A. Gastli, L. Ben-Brahim, N. Al-Emadi, and M. Gabbouj, "Real-time fault detection and identification for MMC using 1-D convolutional neural networks," *IEEE Trans. Ind. Electron.*, vol. 66, no. 11, pp. 8760–8771, Nov. 2019.
[36] S. H. Kim, D. Y. Yoo, S. W. An, Y. S. Park, J. W. Lee, and K.-B. Lee, "Fault detection method using a convolution neural network for hybrid active neutral-point clamped inverters," *IEEE Access*, vol. 8, pp. 140632–140642, 2020.
[37] S. Zhang, R. Wang, Y. Si, and L. Wang, "An improved convolutional neural network for three-phase inverter fault diagnosis," *IEEE Trans. Instrum. Meas.*, vol. 71, Nov. 2022, Art. no. 3510915.
[38] W. Yuan, Z. Li, Y. He, R. Cheng, L. Lu, and Y. Ruan, "Open-circuit fault diagnosis of NPC inverter based on improved 1-D CNN network," *IEEE Trans. Instrum. Meas.*, vol. 71, Apr. 2022, Art. no. 3510711.
[39] W. Sun, R. Zhao, R. Yan, S. Shao, and X. Chen, "Convolutional discriminative feature learning for induction motor fault diagnosis," *IEEE Trans. Ind. Inform.*, vol. 13, no. 3, pp. 1350–1359, Jun. 2017.
[40] W. Gong, H. Chen, Z. Zhang, M. Zhang, and H. Gao, "A data-driven-based fault diagnosis approach for electrical power DC-DC inverter by using modified convolutional neural network with global average pooling and 2-D feature image," *IEEE Access*, vol. 8, pp. 73677–73697, 2020.
[41] L. Wen, X. Li, L. Gao, and Y. Zhang, "A new convolutional neural network-based data-driven fault diagnosis method," *IEEE Trans. Ind. Electron.*, vol. 65, no. 7, pp. 5990–5998, Jul. 2018.
[42] Q. Yang, J. Zhang, L. Chen, and D. Wu, "Fault diagnosis of motor bearing based on improved convolution neural network based on VMD," in *Proc. IEEE 31th Chin. Control Decis. Conf.*, 2019, pp. 405–409.
[43] M. Lin, Q. Chen, and S. Yan, "Network in network," in *Proc. 2nd Int. Conf. Learn. Representations*, 2014, pp. 1–10.
[44] P. Gao, C. Chen, and S. Qin, "An optimization method of hidden nodes for neural network," in *Proc. 2nd Int. Workshop Educ. Technol. Comput. Sci.*, 2010, pp. 53–56.
[45] L. Zhang, J. Jiang, P. Liu, Y. Liang, and R. Yu, "Multivariate nonlinear modelling of fluorescence data by neural network with hidden node pruning algorithm," *Analytica Chimica Acta*, vol. 344, no. 9, pp. 29–39, 1997.
[46] H. Shao, H. Jiang, Y. Lin, and X. Li, "A novel method for intelligent fault diagnosis of rolling bearings using ensemble deep auto-encoders," *Mech. Syst. Signal Process.*, vol. 102, no. 1, pp. 278–297, Mar. 2018.
[47] L. van der Maaten and G. Hinton, "Visualizing data using t-SNE," *J. Mach. Learn. Res.*, vol. 9, no. 11, pp. 2579–2605, 2008.

Borong Wang (Member, IEEE) received the B.S. and M.S. degrees from the Qingdao University of Technology, Qingdao, China, in 2012 and 2016, respectively, and the Ph.D. degree in electrical engineering from Zhejiang University, Hangzhou, China, in 2022.

In 2022, he joined Shanghai Electric Group Company, Ltd., as a Power Electronics System Engineer. His current research interests include converter topologies, fault diagnosis and recovery for power electronic system, and control and stability analysis of grid-connected inverters.

Guodong Chen received the B.S. and M.S. degrees in electrical engineering from Tongji University, Shanghai, China, and the Ph.D. degree in power electronics from Shanghai Jiao Tong University, Shanghai, China, in 2003, 2006, and 2014, respectively.

Since 2006, he has been with Shanghai Electric Power Transmission and Distribution Group, where he is currently the Chief Engineer of power electronics with Shanghai Electric Group Company, Ltd. His current research interests include power quality systems and energy storage systems.

Jinfeng Song received the B.S. and M.S. degrees in electrical engineering from the University of Shanghai for Science and Technology, Shanghai, China, in 2005 and 2008, respectively. He is currently working toward the Ph.D. degree in electrical engineering with Shanghai Jiao Tong University, Shanghai, China.

He is currently a Senior Engineer with Shanghai Electric Group Company, Ltd., Shanghai, China. His current research interests include power quality systems, energy storage systems, and renewable energy power conversion systems.

Chenyi Peng received the B.S. and Ph.D. degrees in electrical engineering from Tongji University, Shanghai, China, in 2012 and 2017, respectively.

She is currently a Senior Engineer with Shanghai Electric Group Company, Ltd., Shanghai, China. Her current research interests include the high-frequency magnetic technology and the renewable energy power conversion.

Philip T. Krein (Life Fellow, IEEE) received the B.S. degree in electrical engineering and the A.B. degree in economics and business from Lafayette College, Easton, PA, USA, in 1978, and the M.S. and Ph.D. degrees in electrical engineering from the University of Illinois at Urbana–Champaign, Champaign, IL, USA, in 1980 and 1982, respectively.

He was an Engineer with Tektronix, Beaverton, OR, USA, and then returned to the University of Illinois at Urbana–Champaign. He was a Senior Fullbright Scholar with the University of Surrey, Guildford, U.K., from 1997 to 1998. From 2003 to 2014, he was a Founder and the Director of SolarBridge Technologies, Inc., Austin, TX, USA, a developer of ac photovoltaic panels. From 2016 to 2020, he was the Executive Dean of the Zhejiang University, Haining, China, and the University of Illinois at Urbana–Champaign Institute. He holds the Grainger Endowed Chair Emeritus in Electric Machinery and Electromechanics with the University of Illinois at Urbana–Champaign. He holds 42 U.S. patents and is a Registered Professional Engineer in Illinois and Oregon. His current research interests include all aspects of power electronics, machines, drives, and electric transportation, with emphasis on nonlinear control approaches.

Dr. Krein was a recipient of the IEEE William E. Newell Power Electronics Award in 2003 and the IEEE Transportation Technologies Award in 2021. He is the past President of the IEEE Power Electronics Society, a past member of the IEEE Board of Directors, and a past Chair of the IEEE Transportation Electrification Community. He is an Associate Editor for the IEEE *Open Journal of Power Electronics*. He is a Fellow of the U.S. National Academy of Inventors and a member of the U.S. National Academy of Engineering.

Hao Ma (Senior Member IEEE) received the B.S., M.S., and Ph.D. degrees in electrical engineering from Zhejiang University, Hangzhou, China, in 1991, 1994, and 1997, respectively.

Since 1997, he has been a Lecturer, an Associate Professor, and a Professor with Zhejiang University. From 2007 to 2008, he was a Delta Visiting Scholar with North Carolina State University. He is the Vice Dean with Zhejiang University, Haining, China, and the University of Illinois at Urbana–Champaign Institute, Champaign, IL, USA. He has authored two books and has authored or coauthored more than 300 technical papers. His current research interests include advanced control in power electronics, wireless power transfer, fault diagnosis of power electronic circuits and systems, and application of power electronics.

Dr. Ma is currently the Vice President of China Power Supply Society. He was an Associate Editor for the *IEEE Journal of Emerging and Selected Topics in Power Electronics* and the *Journal of Power Electronics*. He was the AdCom member of the IEEE Industrial Electronics Society, the Technical Program Chair of the 2012 IEEE International Symposium on Industrial Electronics, the 2014 IEEE International Power Electronics and Application Conference and Exposition (PEAC), IEEE PEAC 2018, and IEEE PEAC 2022.